PECULIARITIES OF 630.0 AND 557.7 nm EMISSIONS IN THE MAIN IONOSPHERIC TROUGH: MARCH 17, 2015

N.A. Zolotukhina
Institute of Solar-Terrestrial Physics SB RAS,
Irkutsk, Russia, zolot@iszf.irk.ru

N.M. Polekh
Institute of Solar-Terrestrial Physics SB RAS,
Irkutsk, Russia, polekh@iszf.irk.ru

A.V. Mikhalev
Institute of Solar-Terrestrial Physics SB RAS,
Irkutsk, Russia, mikhalev@iszf.irk.ru

A.B. Beletsky
Institute of Solar-Terrestrial Physics SB RAS,
Irkutsk, Russia, beletsky@iszf.irk.ru

S.V. Podlesny
Institute of Solar-Terrestrial Physics SB RAS,
Irkutsk, Russia, step8907@mail.ru

Abstract. Peculiarities of 557.7 and 630.0 nm emissions observed in the second step of the magnetic storm main phase at the mid-latitude observatory Tory (52° N, 103° E) on March 17, 2015 are compared with the changes in ionospheric parameters above this station, detected from ionospheric sounding data and total electron content maps. We have found that the intensity of the 557.7 and 630.0 nm emissions noticeably increased after the observatory entered into the longitudinal sector of the developed main ionospheric trough (MIT). The most powerful synchronous increases in intensities of the two emissions are associated with amplification of the westward electrojet during strengthening of the magnetospheric convection. We study the dependence of the ratios between the intensities of 630.0 nm emission recorded in the north, zenith, and south directions on the position of emitting regions relative to the MIT bottom. The SAR arc is shown to appear initially near the bottom of the MIT polar wall and approach the zenith of the station during registration of F3s reflections by an ionosonde, which indicate the presence of a polarization jet near the observation point.

Keywords: second step of the magnetic storm main phase, 557.7 and 630.0 nm emissions, main ionospheric trough, polarization jet.

INTRODUCTION

During night hours on March 17, 2015, the complex of optical instruments installed in the ISTP SB RAS Geophysical Observatory ISTP (GPhO, the village of Tory, geographic coordinates φ=52° N, λ=103° E, corrected geomagnetic latitude φ'=47.9°) detected intense 557.7 and 630.0 nm atomic oxygen emissions, defined as mid-latitude aurora [Mikhalev et al., 2018; Mikhalev, 2019]. On the basis of space-time dynamics of the intensities, the authors of the above papers have concluded that the synchronous bursts of 557.7 and 630.0 nm emissions, which lasted for about an hour, observed on that day were type «a» auroras; and the slowly varying 630.0 nm emission component was represented by diffuse airglow and/or type «d» aurora, as well as by a stable auroral red arc (SAR arc). Note that mid-latitude auroras are the auroras that are observed from regions far below the «typical auroral zone» [Suzuki et al., 2015].

According to the information collected to date, the aurora types identified in [Mikhalev et al., 2018; Mikhalev, 2019] are associated with the electron fluxes of specific energies precipitating into the atmosphere from various magnetospheric regions [Bame et al., 1967; Rassoul et al., 1993; Frey, 2007; Feldstein et al., 2010; Feldstein et al., 2014; Mishin et al., 2018; Mikhalev, 2019]. Type «a» auroras are excited by electrons with energies ~0.1–10 keV, which come to the auroral oval from the central plasma sheet after significant acceleration. The criteria used to identify the central plasma sheet are discussed, for example, in [Baumjohann et al., 1989]. Diffuse auroras are caused by electrons with 0.01–1 keV energies coming from the plasma sheet to ionospheric heights without acceleration [Starkov, 2000]. Note that the diffuse auroras are observed in an extended latitudinal region, projected along the magnetic field onto the entire central plasma sheet [Ni et al., 2016]. Type «d» auroras and SAR arcs occur when electrons with energies ~0.01–1 and ≤0.01 keV respectively, which precipitate from the plasmapause region, have an effect on the atmosphere [Rassoul et al., 1993]. At ionospheric heights, to the diffuse auroral zone (diffuse precipitation) corresponds the polar wall of the main ionospheric trough (MIT); and to the plasmapause, its equatorial wall [Khalipov et al., 1985; Feldstein et al., 2010; Mendillo et al., 2013; Deminov, 2015].

Figure 1, *a*, *b* shows that the optical data analyzed was obtained during the main phase of a two-step magnetic storm (two-step storm main phases [Gonzalez et al., 2002]), namely at its second step (the second decrease in *Dst*). At the beginning of this step, from 12:00 to 13:00 UT, the cross-polar cap potential drop increased from 50 to more than 150 kV and remained large until the end of March 17 [Hairston et al., 2016]. In the Northern Hemisphere at 15:00–16:00 UT, the sunward convection moved as far as the corrected geomagnetic latitude φ'~30–40°/40–50° in dusk/dawn sectors
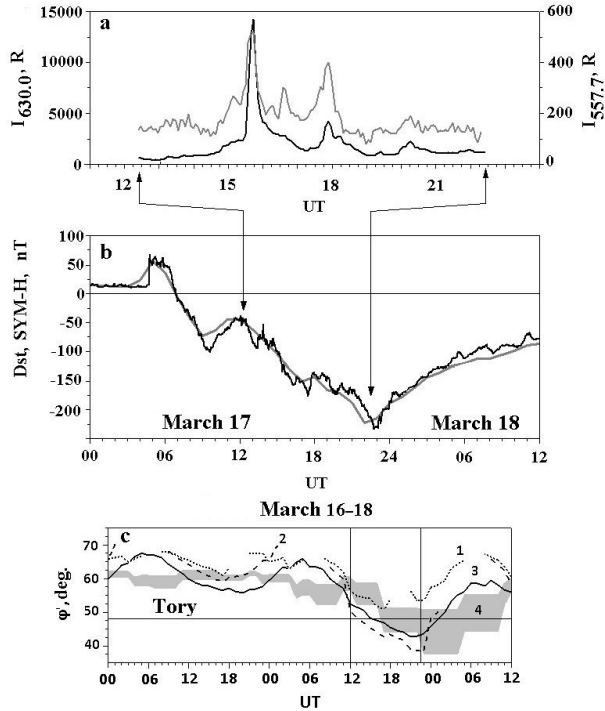
Figure 1. Variations in 630. 0 and 557.7 nm emission intensities (black and gray lines) in a northerly direction, measured by a patrol spectrograph on March 17, 2015 (*a*); in *SYM-H* and *Dst* (black and gray lines) (*b*); in corrected geomagnetic latitudes φ' of the equatorial edge of diffuse precipitation zone (1), MIT bottom (2, 3), and plasmapause (4), determined for the meridian of 105° E by the models developed in [Gussenhoven et al., 1983; Zherebtsov et al., 1986; Deminov, Shubin, 2018; Moldwin et al., 2002] (*c*). Vertical lines indicate the beginning and the end of optical observations (12:00–22:30 UT, March 17); the horizontal line is the GPhO latitude (Tory)

[Hairston et al., 2016]; the nightside auroral oval expanded to φ'~50° [Le et al., 2016; Kosar et al., 2018]; centers of auroral electrojets shifted to φ'~55° [Jacobsen, Andalsvik, 2016; Zolotukhina et al., 2016; Zolotukhina et al., 2017]. At around the same time, MIT shifted at λ=120 °E to φ=52° N (φ'~48°) [Polekh et al., 2016], and the 557.7 ($I_{557.7}$) and 630.0 nm ($I_{630.0}$) emission intensities, observed at GPhO in a northerly direction, sharply increased to maximum values of ~0.5 and 14 kR respectively for the event considered [Mikhalev et al., 2018; Mikhalev, 2019].

Results of the calculations (Figure 1, *c*) made by empirical models, based on K_p or *ap* indices, for the 105° E meridian close to GPhO show that on March 17 the latitudes of the diffuse precipitation zone equatorial edge, MIT bottom, and plasmapause might have been by 10°–20° lower than at the same hours on March 16. In this case, at 15:00–18:00 UT (22:00–01:00 LT) the boundary of diffuse precipitation might have been by 3°–5° northward of GPhO; and the plasmapause and the MIT bottom from 15:00 UT (22:00 LT), near it or southward of it.

The MIT shift to midlatitudes is a rare event. Calculations made by the model [Deminov, Shubin, 2018] suggest that at λ=105° E the MIT bottom can shift to φ'=50° at dusk only when $K_p \geq 8$ ($ap \geq 207$), i.e. during severe and extreme magnetic storms [https://www.swpc.noaa.gov/noaa-scales-explanation].

Even more rare are the cases of occurrence of auroras with intensities higher than 1 kR at midlatitudes because their observation is limited to night hours and weather conditions (clouds). For example, during the past two solar cycles GPhO has detected only seven such cases. All of them occurred during severe and extreme magnetic storms with minimum *Dst*<–222 nT, including the storm we analyze [Mikhalev, 2019].

Hence it becomes relevant to study the relationship between the dynamics of mid-latitude auroras and magnetospheric-ionospheric disturbances for each individual case. In this paper, we conduct this research for the auroras observed by GPhO on March 17, 2015 at the second step of the geomagnetic storm main phase, i.e. during secondary ring current amplification. Our main purpose is to examine relationships between the dynamics of auroral airglows and that of MIT structural elements. To solve this problem, we will carry out a comparative analysis of the space-time dynamics of intensities of the 557.7 and 630.0 nm emissions observed at GPhO, changes in ionospheric parameters over this observatory, the total electron content (TEC) along the 105° E meridian, and geomagnetic disturbances observed eastward and westward of GPhO.

1. DATA AND METHODS

1.1. The optical data in use has been acquired at the complex of instruments described in [Mikhalev et al., 2018]. For quantitative analysis, we have used values of I_N, I_Z, I_S (630.0 nm emission intensities) and T_N, T_Z, T_S (Doppler temperatures determined for the 630.0 nm line), measured with the Fabry—Perot interferometer (FPI) in the north, zenith, and south directions respectively [Vasilyev et al., 2017]. In addition, we have analyzed variations in intensities of the 557.7 and 630.0 nm emissions ($I_{557.7}$ and $I_{630.0}$), estimated by the patrol spectrograph for the atmospheric research (SATI-1M) at 63°–71° zenith angles [Mikhalev et al., 2018]. Over the period considered, FPI (3° aspect angle) worked at a wavelength of 630.0 nm in a mode of patrol survey of five directions — cardinal points (elevation angle ψ=30°, sampling period Δt=254 s), and zenith (ψ=90°, Δt=127 s). The patrol spectrograph (ψ~23°, ~8° inclination to the geographic meridian, ~25° angular field of view, Δt=260 s) was oriented to the north.

Images taken by an all-sky camera KEO Sentinel (viewing direction is zenith, 145° field of view, 30 s exposure time; spectrophotometric calibration was performed from starry sky images [Shindin et al., 2017]) were used to analyze the space-time dynamics of the SAR arc; those taken by a wide-angle color camera FILIN-1Ts (~85° angular field of view, 300 s exposure time), to study spatio-temporal variations in midlatitude emissions. In the north, the FILIN-1Ts field of view is limited by the Sayan Mountains (ψ~10.5°).

1.2. According to different literature sources, the 557.7 and 630.0 nm emissions are excited at heights h=90–240 km and h=150–400 km respectively; and SAR arcs, at h=400–450 km [Alekseev et al., 1975; Khomich et al., 2008; Zverev et al., 2012; Mendillo et al., 2013; Feldstein et al., 2014; Tashchilin, Leonovich 2016; Megan Gillies et al., 2017; Aruliah et al., 2019].

Following [Mendillo et al., 2013], we assume that 630.0 nm emission intensity peaks at h=200 km (diffuse airglows) and h=400 km (SAR arcs); whereas the 557.7 nm emissions, at h=100 km.

In the spherically stratified approximation at these heights and at the angles mentioned in Section 1.1, SATI-1M obtained data from latitudes spaced apart from the GPhO latitude by $\Delta\varphi'$~1.7°–2.4° (557.7 nm emission), $\Delta\varphi'$=3.2°–4.5° (diffuse airglows), and 6°–8° (SAR arc). The FPI data from the north and south directions corresponds to the regions spaced away from GPhO by $\Delta\varphi'$~2.9° at h=200 km and 5.4° at h=400 km. To the zenith direction correspond the GPhO latitude (φ'= 47.9°) and the 103° E longitude. The KEO Sentinel camera field of view is limited in the north and south to $\Delta\varphi'$=5.1° at h=200 km and to $\Delta\varphi'$=9° at h=400 km; and that of the camera FILIN-1Ts, in the north to $\Delta\varphi'$=4.2° at h=100 km, $\Delta\varphi'$=6.3° at h=200 km, and $\Delta\varphi'$=10.8° at h=400 km.

1.3. The study is based on the values of interplanetary medium parameters and geomagnetic activity indices from [http://cdaweb.gsfc.nasa.gov/istp_public]. From the same website, we took data on variations in the geomagnetic field H component, directed to the geomagnetic pole, from the observatories Tiksi and Dikson, (for THEMIS with a sampling period Δt=60 s) and TEC time series with latitudinal, longitudinal, and temporal resolutions of 2.5°, 5°, and 15 min respectively (for GPS-deduced 15-minute Total Electron Content (TEC) global maps). The values of the geomagnetic field X, Y, and Z components (directed respectively to the north geographic pole, to the east, and vertically downward), measured at the observatories Yakutsk, Da Lat, and Phu Thuy with Δt=60 s, are from [https://www.intermagnet.org/data-donnee/download-eng.php]; GOES-13, -15 magnetic data with Δt=60 s, from [ftp.swpc.noaa.gov/pub/warehouse].

The MIT dynamics was examined using TEC distributions, often applied for this purpose [Pryse et al., 2006; Mendillo, 2006; Shinbori et al., 2018], values of F2-layer critical frequencies (f_oF2), and F-region minimum virtual heights ($h'F$). These values were obtained with one-minute resolution by the manual processing of ionograms from a chirp ionosonde installed in GPhO [Podlesnyi et al., 2013].

Auroral precipitation energy flux density distributions (ε) have been constructed using data from [https://www.ngdc.noaa.gov/stp/ovation_prime/data] (calculated from the model [Newell et al., 2009]). To determine the latitude of the equatorial boundary of diffuse precipitation, the criterion ε=0.2 erg/(cm$^2\cdot$s) [Ding et al., 2017; Kosar et al., 2018] has been adopted. For convenience, according to the features of intensity variations, we have selected eight UT intervals (13:00–14:30 (1), 14:30–15:25 (2), 15:25–16:00 (3), 16:00–17:10 (4), 17:10–19:00 (5), 19:00–19:45 (6), 19:45–21:10 (7), 21:10–22:00 (8). Boundaries of the intervals are marked in the Figures with vertical dashed lines; their numbers are at the top of the panels.

2. MIT DYNAMICS AT THE GPhO MERIDIAN

2.1. During optical observations made at 12:00–22:30 UT on March 17, 2015, GPhO went through the 19:00–05:30 LT sector. Figure 1 shows that noticeable changes in $I_{630.0}$ and $I_{557.7}$ occurred after 13:00 UT. From 13:07 to 13:16 UT, $I_{630.0}$ increased by ~300 R, and in the plot of $I_{557.7}$ (UT) appeared oscillations with 30–50 R amplitude (~20–30 % of mean $I_{557.7}$~150 R at 13:00–14:00 UT). Figure 2 (panel 2) indicates that at 13:00 UT in the TEC distribution along the 105° E meridian equatorward of the auroral precipitation zone (auroral oval), a structure consisting of three elements peculiar to MIT — TEC minimum (bottom), polar and equatorial walls — emerged [Pryse et al., 2006]. Note that MIT differs from other high-latitude troughs in that it is located equatorward of the oval [He et al., 2011]. An hour before, at 12:00 UT (panel 1 in Figure 2), there was no structure similar to MIT at λ=105° E.

2.2. Changes of the MIT bottom latitude, determined from TEC profiles, and the latitude of the equatorial edge of the diffuse precipitation zone are displayed in Figure 3, *a*. In those cases when minimum TEC was observed at one point (see, e.g., panels 2, 4 in Figure 2), the latitude of the MIT bottom is marked with squares. If the TEC values that differ by no more than 5 % from the minimum one are seen at several adjacent points (see panels 5, 6, 8 in Figure 2), their latitudes are joined by rectangles. The TEC values around the MIT bottom were 10–75 % lower than those at the top of the polar wall. Dark gray squares (rectangles) in Figure 3, *a* are TEC decreases by 25–75 % at the bottom; light gray ones, by 10–24 %. The MIT depth was maximum at 15:30–15:45 UT.

On the basis of the MIT bottom motions, shown in Figure 3, *a*, and considering that TEC maps have a latitudinal resolution of 2.5°, we believe that at 15:30–17:30 UT GPhO was near the MIT bottom and then in a broad zone of low TEC, which might have also been an MIT bottom. An expansion of MIT and a decrease in its depth after midnight, similar to that illustrated in panels 6–8 of Figure 2, are described in [Pryse et al., 2006].

2.3. The fact of shift of an MIT-like structure to the GPhO latitude, which has been inferred from TEC distributions, is confirmed by the ionospheric sounding data shown in Figure 3, *b*, *c*. We can see that at 12:00 UT (19:00 LT) GPhO was under a positive ionospheric disturbance, which completely disappeared by 14:00 UT. During the decrease in the MIT bottom latitude, inferred from TEC distributions, from φ'~53.5° at the end of interval 1 to φ'~48.5–51° at the beginning of interval 3, GPhO observed the f_oF2 and $h'F$ variations typical of MIT. From 14:15 to 15:30 UT, the F2-layer critical frequency decreased by ~2 MHz, and $h'F$ gradually increased by ~240 km. After 15:30 UT and until the end of the day, f_oF2 was by ~2 MHz lower and $h'F$ by 100–200 km higher than background ones.
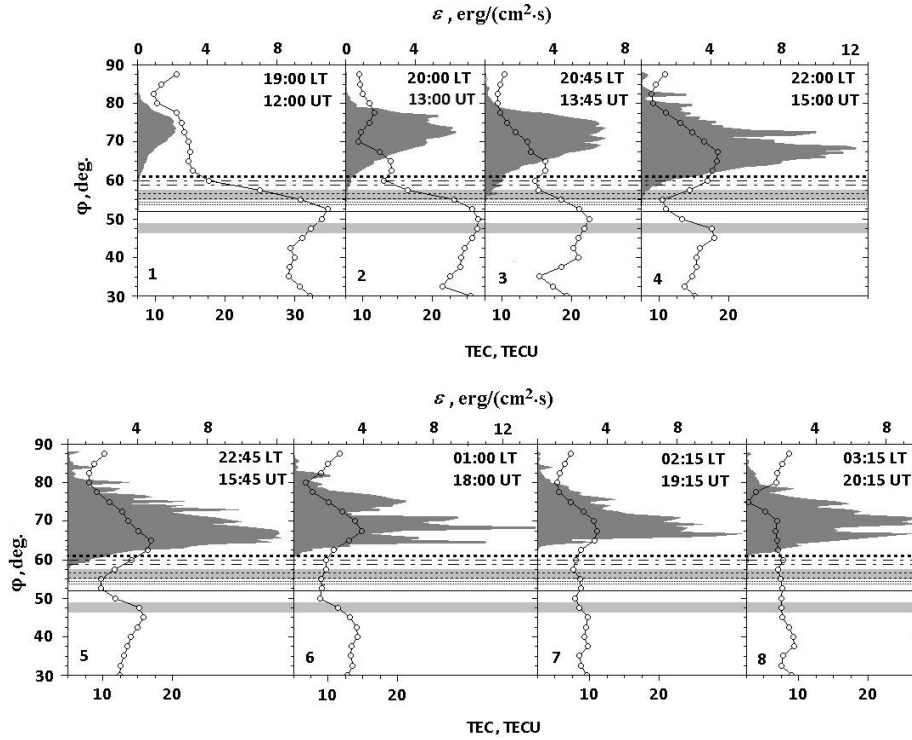
ε , erg/(cm^2·s)

Figure 2. Examples of latitudinal TEC distributions built for March 17, 2015 (lines with open circles) and ε (solid gray figures) at the 105° E meridian. In this and other Figures, gray stripes mark latitudes of the areas covered by the FPI field of view at h=200–400 km; pairs of dash-dotted and dotted lines, areas falling within the SATI-1M field of view at 400, 200, and 100 km respectively. Thick solid black and dotted lines indicate latitudes of GPhO and the north horizon of the KEO Sentinel camera at h=400 km
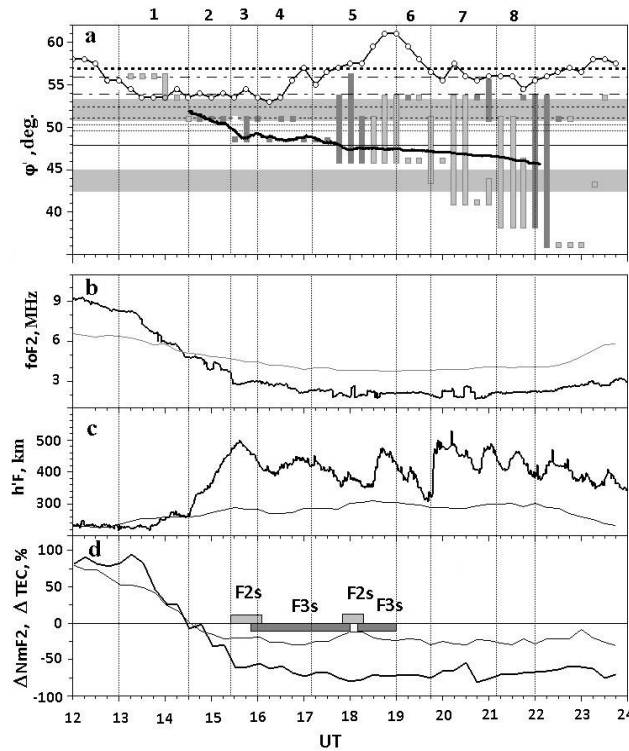
Figure 3. Changes on March 17, 2015 in corrected geomagnetic latitudes of the equatorial edge of the diffuse precipitation zone, calculated by the model [Newell et al., 2009] (line with open circles), the MIT bottom (squares and rectangles), and the SAR-arc center (thick line) (*a*); current/background (black/gray line) values of f_oF2 (*a*) and h'F2 (*b*) (*b*, *c*); normalized deviations of N_mF2 and TEC (black and gray lines) from background values (*d*). The background values of f_oF2, h ,2F'N_mF2 are equal to their average values obtained on March 13–15. In panel *d*, light gray and dark gray rectangles indicate intervals of detection of F2s and F3s reflections respectively. Vertical lines mark boundaries of the intervals, differing in characteristics of geomagnetic disturbances and airglows observed in them

Reflections from the regular (background) F2 layer are visible in all ionograms obtained simultaneously with optical measurements. Until 15:18 UT, the ionograms had no significant interference. Reflections from the F2 layer became diffuse after a sharp decrease in f_oF2 (by 1 MHz for 5 min) at the beginning of interval 3, which occurred against maximum h'F. In addition there are oblique reflections with higher frequencies, as compared to reflections from the regular F2 layer, and approximately the same delays in ionograms obtained at 15:25–16:05 and 17:50–18:17 UT. These reflections are similar to the F2s reflections presented in [Filippov et al., 1984; Stepanov et al., 2017]. At 15:52–18:00 and 18:08–19:00 UT, the iongrams exhibit F3s reflections — additional tracks lying within lower frequencies and longer delays than those from the F2 layer [Filippov et al., 1984; Stepanov et al., 2017]. In Figure 3, *d*, the intervals of observation of the F2s and F3s reflections are marked with light gray and dark gray rectangles. Occurrence of F2s reflections in intervals 3 and 5 implies that the MIT polar wall is near a point of observation; and F3s reflections in intervals 4 and 5 indicate a narrow ionization trough in the polarization jet region [Filippov et al., 1984; Stepanov et al., 2017].

Figure 3, *d* compares plots of normalized deviations of the F2-layer maximum electron density and TEC (ΔN_mF2 and ΔTEC) from their background values: ΔN_mF2 are determined from f_oF2 (N_mF2=$1.24\cdot10^4\cdot f_o$F2^2 см$^{-3}$); ΔTEC, from TEC values at the point with coordinates φ=52.5°, λ=105°. The trends in ΔN_mF2 and ΔTEC are similar, but after 15:30 UT the depth of decrease in N_mF2 (~60–75 %) is 3–4 times greater than that in TEC (~15–25 %). This means that the trough in the F2-layer maximum electron density might have been deeper than that in TEC. The manifestations of ionospheric disturbances identified indicate that after 15:25 UT GPhO entered the MIT zone and possibly remained in it until the end of the day.

3. GEOMAGNETIC DISTURBANCES IN THE SECTOR OF OPTICAL OBSERVATIONS

3.1. Figure 4 compares $I_{557.7}$ and $I_{630.0}$ variations with variations in the horizontal magnetic field component at high latitudes. In the time interval considered at the observatories Tiksi (φ=71.6° N, λ=128.8° E, φ'=66.5°) and Yakutsk (φ=62° N, λ=127.9° E, φ'=56.8°), located by ~25° eastward of GPhO, and at the observatory Dikson (φ=73.5° N, λ=80.7° E, φ'=69.4°), located by ~22° westward of it, there were multiple negative disturbances in the *X* (Yakutsk) or *H* (Tiksi, Dikson) component of the geomagnetic field. Therefore, GPhO was all this time in the sector of the westward electrojet.

3.2. The $\Delta H_{\text{DLT-PHU}}$ variations (Figure 4, *a*), i.e. differences between the horizontal geomagnetic field components ($H=(X^2+Y^2)^{1/2}$) measured at the observatories Da Lat (φ=11.9° N , λ=108.5° E, 2.19° inclination) and Phu Thuy (φ=21° N, λ=106° E, 11.2° inclination), provide information about the direction of electric field near the meridian of magnetic, and in our case also optical, measurements [Blanc, Richmond, 1980; Balan et al., 2010; Polekh et al., 2017]. The gray stripe shows limits of the $\Delta H_{\text{DLT-PHU}}$ variation during magnetically quiet days on March 13–15; the black line indicates current values on March 17. Significant, ~10 nT deep, decreases in current values of $\Delta H_{\text{DLT-PHU}}$ relative to the gray stripe in intervals 3, 5, and 7 suggest that the enhanced magnetospheric convection field, directed to the west at night, in them was greater than the eastward field of disturbed dynamo.

3.3. Strong amplifications in the western electrojet, which appeared as deep bay-like depressions in *H* or *X* component of the geomagnetic field, were sequentially fixed in intervals 1, 3, 5, and 7. During a substorm with multiple onsets [McPherron, 1978; Nagai et al., 1983], developed in interval 1, the greatest amplification in the field of the westward electrojet with ΔH~–2000 nT was detected at the auroral observatory Dikson at ~13:40 UT, after the transition from positive to weak negative disturbance of the geomagnetic field *Z* component (points to the shift of the westward electrojet center from south to north with respect to the observatory). In interval 2, the *H* component in Tiksi and Dikson gradually returned to its pre-substorm level, and the *X* component in Yakutsk non-monotonically decreased. It reached a minimum (ΔX~–1700 nT) at ~15:40 UT in interval 3, in which, as the bay-like decrease in $\Delta H_{\text{DLT-PHU}}$ implies, the magnetospheric convection field strengthened, whereas the westward electrojet center shifted to the lowest latitudes and was near Yakutsk [Zolotukhina et al., 2016]. In the same interval there were the highest (among the three pairs of peaks observed by SATI-1M) synchronous peaks of $I_{630.0}$ and $I_{577.7}$.

The $\Delta H_{\text{DLT-PHU}}$ decreases in intervals 5 and 7 also coincide in time with the synchronous peaks of $I_{630.0}$ and $I_{577.7}$, which are smaller than in interval 3, and with the bay-like geomagnetic field depressions, which are the deepest (ΔH~–1700 and –1200 nT) at the Observatory Dikson. In contrast, the first, the most intense according to data from the Observatory Dikson, substorm, observed in interval 1, was not accompanied by noticeable changes in the equatorial electric field and by synchronous increases in $I_{630.0}$ and $I_{577.7}$.

4. RELATIONSHIP BETWEEN OPTICAL, GEOMAGNETIC, AND IONOSPHERIC DISTURBANCES

4.1. Images taken with the FILIN-1Ts and KEO Sentinel cameras show that near their northern horizons in intervals 1, 5, 7 there were bright discrete structures moving from west to east. The direction of motion of the structures suggests that their primary sources related to substorms were located westward of GPhO (Section 3.3). In interval 3 were bright red vertical flashes of aurora borealis. Relying on the estimated distances to northern horizons of SATI-1M, FILIN-1Ts (Section 1.2) and the variations in the latitude of the equatorial
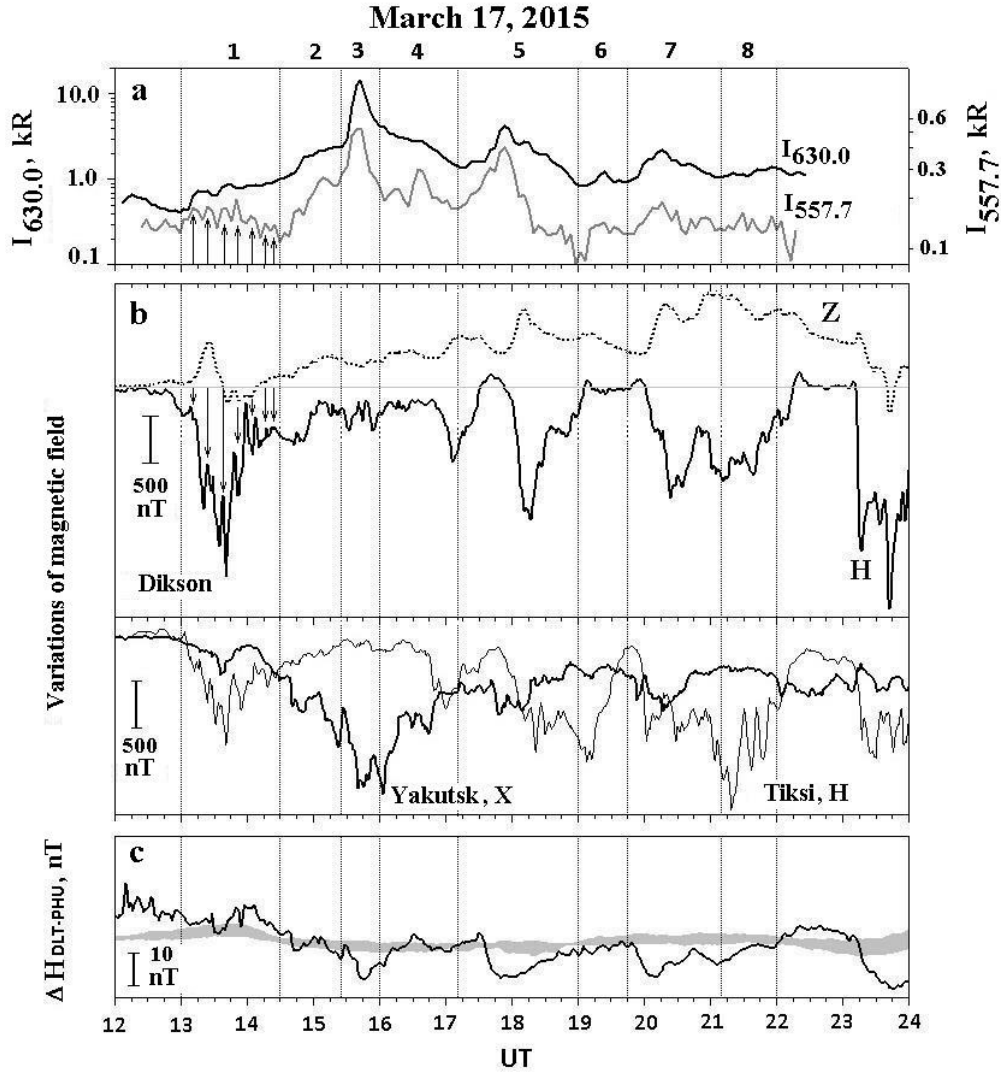
Figure 4. Variations in: the intensity of 630. 0 and 557.7 nm emissions (black/gray line) as derived from SATI-1M data (*a*); the *H*, *X*, and *Z* components of the magnetic field at the three high-latitude observatories (*b*); $\Delta H_{DLT-PHU}$ (*c*). In interval 1, vertical arrows denote the relationship between seven quasi-periodic fluctuations of the westward electrojet field and $I_{577.7}$, which have roughly the same duration and time of occurrence.

edge of the diffuse precipitation zone (Figure 3, *a*), we believe that auroral precipitation increases during substorms are responsible for the above discrete structures.

4.2. In Section 3.3, we have noted that distinct synchronous peaks of $I_{557.7}$ and $I_{630.0}$ were seen in intervals 3, 5, 7 during bay-like decreases in the *H* or *X* components of the geomagnetic field, which coincided in time with enhancements of the magnetospheric convection field. In intervals 3, 5, 7, the bursts of $I_{557.7}$ and $I_{630.0}$ were preceded by decreases in the latitude of the equatorial edge of the diffuse precipitation zone, characteristic of the substorm growth phase and onset, which were followed by its increases during the transition from the expansion phase to the recovery phase.

4.3. Comparing the plots in Figure 4, *a*, *b* shows that a clear connection between geomagnetic disturbances and increases in atomic oxygen emissions was also seen in interval 1. The $I_{630.0}$ increase by ~300 R at 13:07–13:16 UT and activation of ~12 min quasi-periodic $I_{557.7}$ fluctuations (Section 2.1) coincide within the time reso-

lution of SATI-1M data with the substorm onset at ~13:05 UT and with the appearance of red spots in the FILIN-1Ts images. Arrows in panels *a*, *b* of Figure 4 indicate that in interval 1 to each of the ~11–12 min $I_{557.7}$ oscillations corresponds one of the multiple amplifications of the westward electrojet with the same period. A clear connection between the $I_{557.7}$ peaks and the *X*-component decreases in Yakutsk is also visible in intervals 2 and 3.

Figure 5 shows that jumps in the solar wind dynamic pressure P_{sw} match geomagnetic field *H*-component fluctuations, recorded at the Observatory Dikson, and *AL*-index variations. We believe that a cause of the multiple amplifications of the westward electrojet (including that beginning in Dikson at ~13:05 UT), the rapid increases in $I_{630.0}$, the activation of $I_{557.7}$ fluctuations, and the appearance of red spots might have been solar wind pressure jumps [Meurant et al., 2004; Keika et al., 2009; Tsurutani et al., 2011].

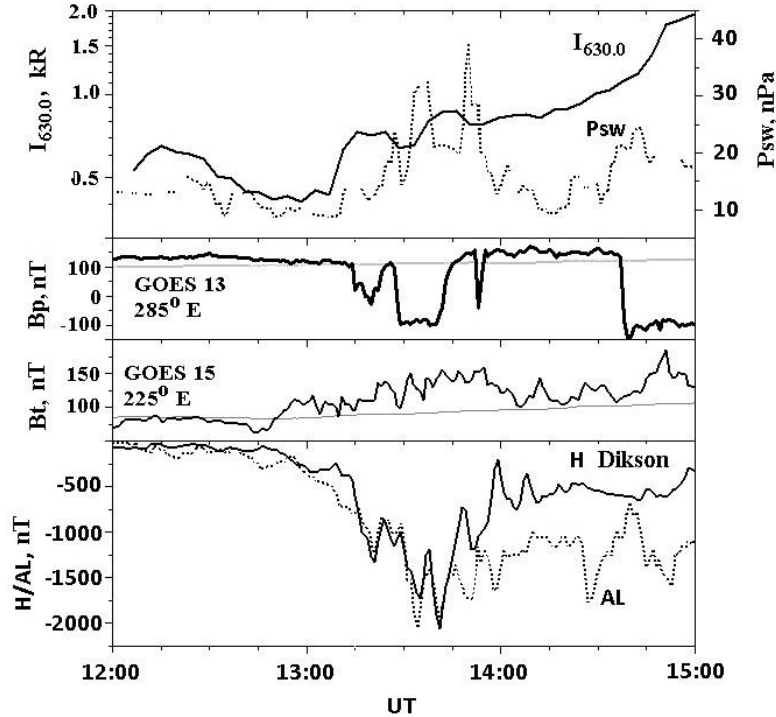The magnetospheric compressions in interval 1 are confirmed by GOES-13 satellite data (λ=285° E): three

Figure 5. Variations (top to bottom) in: $I_{630.0}$ and P_{SW} — solar wind dynamic pressure, the B_p component, parallel to the Earth axis, and the B_t magnetic field modulus, measured by the GOES-13 and -15 satellites respectively, the H component of the geomagnetic field at the Observatory Dikson, and the *AL* index

decreases in the magnetic field B_p component (to –50, –100, and again to –50 нТл) recorded by the satellite at 13:00–14:00 UT (08:00–09:00 LT) suggest that the magnetopause shifted to the satellite's orbit. Magnetospheric compressions generate fast magnetosonic waves propagating isotropically at a velocity of ~1000 km/s, related Alfvén waves, and modulation of magnetospheric-ionospheric currents and precipitating electron fluxes able to penetrate up to h=100–400 km and to increase the 557.7 and 630.0 nm emissions [Meurant et al., 2004]. Figure 5 shows that at 13:00–14:00 UT GOES-15 observed compression waves (quasi-periodic fluctuations in the geomagnetic field modulus B_t) in the sector 04:00–05:00 LT. In the case of interest, the electron population in the shells L~2.5-3.2 (φ'~ 51–56°), adjacent to an area falling within the SATI-1M field of view at h=200–400 km, might have increased at the storm first step (~07:00–10:00 UT).

4.4. Throughout the event of interest, the 630.0 nm emission intensity variations detected by SATI-1M and in a northerly direction by FPI were similar (Figure 6, *a*). The $I_{630.0}$ peaks mentioned in Section 4.2 are close in time to I_N peaks, as well as to increases in I_Z and I_S (Figure 6, *b*). Almost simultaneous increases in I_N, I_Z, and I_S were also recorded at the beginning of interval 1 and during the substorm onset. This confirms the relationship between activations of the westward electrojet during magnetic storms and increases in atmospheric emissions completely covering the field of view of the all-sky camera placed in midlatitudes [Shiokawa et al., 2005].

Nevertheless, the I_N variations and their related T_N variations in intervals 1, 2 are markedly different from those recorded in the zenith and south directions. During the simultaneous increases in I_N, I_Z, I_S, which started at ~13:00, T_N increased by ~100 K, whereas T_Z and T_S remained almost unchanged. To the nonmonotonic increases in I_N at 13:30–15:00 UT corresponded increases in T_N while I_Z, I_S gradually decreased to minimum for the event under study.

The analysis of latitudinal TEC distributions indicates that in early interval 1 an increase in I_N, T_N, and $I_{630.0}$ occurred at latitudes of the northern edge of the positive ionospheric disturbance zone, which coincide with latitudes of the MIT equatorial wall; whereas I_Z, T_Z I_S, T_S variations, inside this zone. At 13:30–14:45 UT, intensity and temperature variations were observed during the transition from positive to negative ionospheric disturbance, i.e. when the ionospheric structure changed in the region studied. By 14:00 UT, ΔN_mF2 and ΔTEC approached zero, and the eastern edge of the region ΔTEC>0, which at 12:00 UT at φ=52.5° occupied the sector 12–23 LT, shifted to ~17:00 LT (λ~45°, Figure 7, *b*). The MIT bottom at λ=105° expanded to φ=57.5° (Figure 7, *a*, left). By 14:45 UT, the base of the equatorial MIT wall approached the FPI field of view in the north direction, and in the zenith direction this wall fell within the FPI field of view (Figure 7, *a*, center). These changes in the MIT structure do not allow us to determine the position of its structural elements relative to FPI fields of view.

4.5. In intervals 1, 2 there are also clear differences between values and variations of T_N and those of T_Z, T_S. Figure 6, *b* shows that at 13:00 UT the Doppler temperature in the north direction only by ~20 K differed from that observed in the south and zenith directions. In interval 1
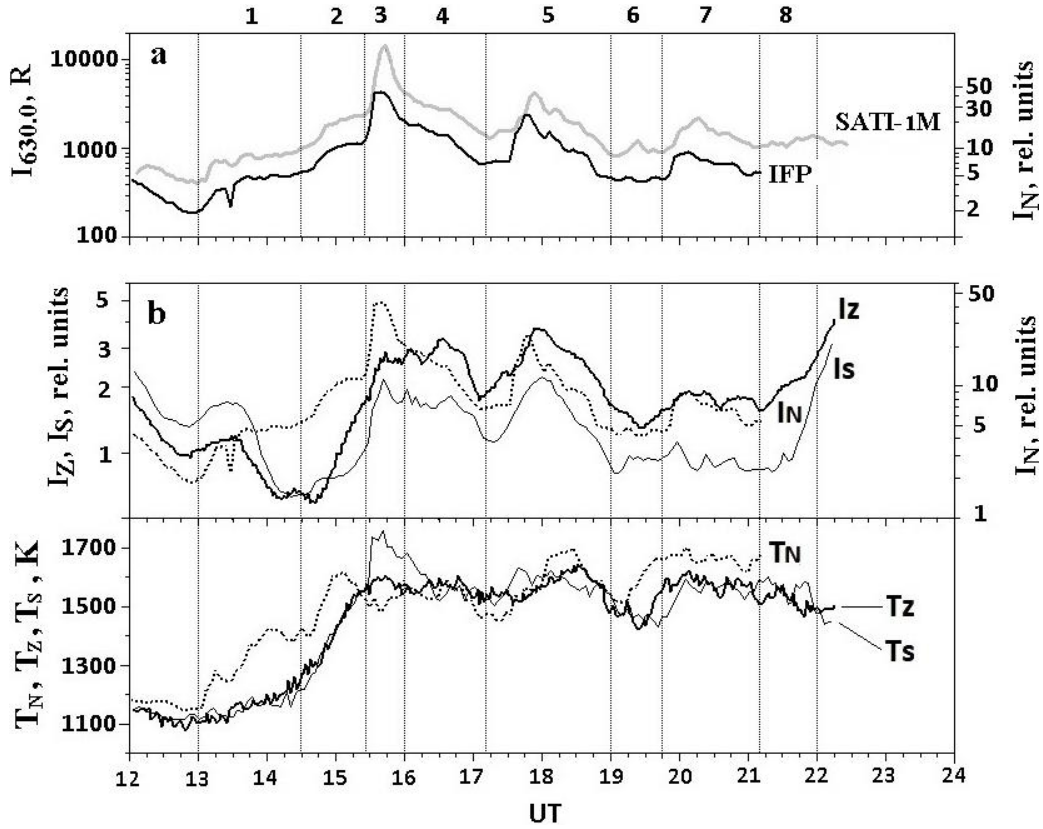
Figure 6. Variations in $I_{630.0}$ and I_N (*a*), intensities and Doppler temperatures in the north, zenith, and south directions (*b*)
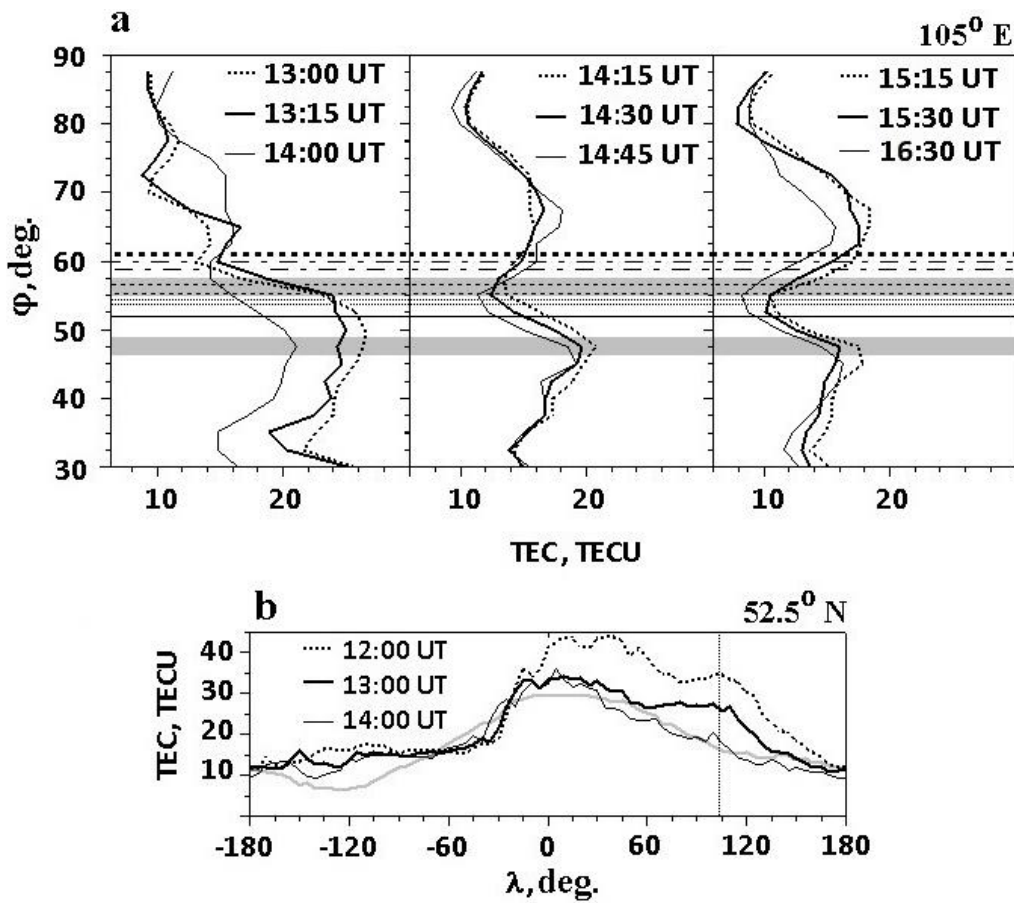

Figure 7. Latitudinal profiles of TEC at the 105° E meridian (*a*) and longitudinal profiles of TEC at a latitude of 52.5° N (*b*) at given moments of time. In panel *b*, the gray line represents background TEC. The vertical dotted line marks the longitude of GPhO

and in the first half of interval 2, smoothly growing T_Z and T_S were by 50–250 K lower than non-monotonically increasing T_N, and became equal to it at the end of interval 2 after the northward Doppler temperature began to decrease. The onset of decrease in T_N at 15:05–15:09 UT coincides (within the temporal resolution of FPI data) with the onset of a two-step decrease in X by 600 nT in Yakutsk at 15:05–15:06 UT or with a northward shift of the MIT polar wall to the latitudes of the FPI field of view.

In interval 3, the Doppler temperature in the areas explored with FPI was maximum in a southerly direction and minimum in a northerly direction. At peak intensities recorded by FPI at 15:35–15:45 UT in all directions, T_N was lower than T_Z and T_S by ~100 and ~250 K respectively. That time, the FPI fields of view in the north and south directions were on either side of the MIT bottom (on its polar and equatorial walls respectively). Thus, in interval 3 the substorm activity enhancement caused $I_{630.0}$ to increase across the MIT zone, and the Doppler temperature to rise (as at the beginning of interval 1) only in the emitting region located near the latitude of the top of its equatorial wall.

After reaching peak values and until the middle of interval 4, I_Z and I_S remained high, whereas I_N decreased threefold. The analysis of latitudinal profiles of TEC, constructed for 16:00–16:30 UT, has shown that the MIT polar wall, its base, and the top of the equatorial wall still persisted in this time period in the FPI field of view in the north, zenith, and south directions respectively. For the next hours, high (low) Doppler temperatures were generally observed concurrently with high (low) intensities. An exception is the rise in T_N by 150 K, which began at 19:14 UT — 19 min before a sharp increase in I_N.

4.6. Figure 8 indicates that the Doppler temperature variations at the zenith of GPhO are similar to variations in the minimum virtual height of the ionospheric F-region over this station. After 16:00 UT, the closest similarity between the T_N and $h'F$ variations is observed if the T_N plot is shifted by ~10 min along the time axis. Thus, a rise in the F-region virtual height follows an increase in the Doppler temperature of oxygen atoms, determined from the broadening of the 630.0 nm line. This suggests that the key factor contributing to the strengthening of this emission after 16:00 UT is the increased temperature in the region of the modified atmosphere composition and/or in the polarization jet band [Bryunelli, Namgaladze, 1988; Khalipov et al., 2018]. It is also deemed that during geomagnetic disturbances due to increasing energy exchange between the plasmasphere and the ring current, at midlatitudes the electron temperature rises at F-region heights [Khomich et al., 2008]. The mechanism for strengthening the 630.0 nm emission in the case of high temperature might be oxygen atom collisions with thermal electrons in the reaction $O(^3P)+e \rightarrow O(^1D)+e$ in addition to the dissociative recombination reaction, which is essential for the excitation of the 630.0 nm emission under quiet geomagnetic conditions.

4.7. Figure 9, *a* displays changes in the ratio $I_{630.0}/I_{557.7}$, calculated from SATI-1M data; Figure 9, *b*, in I_N/I_Z, $I_N/(2I_Z)$, and I_N/I_S, derived from FPI data. Solid lines in Figure 9, *b* represent measured intensities; dotted lines are drawn taking into account the fact that at an elevation angle of 30° the beam length crossing the emitting region is twice as long as at the zenith.

It is thought that the ratio $I_{630.0}/I_{557.7}$ can be used to identify the aurora type [Rassoul et al., 1993]. Mikhalev et al. [2018] have justly noted, however, that during the March 17, 2015 storm the patrol spectrograph made measurements «at small angles above the horizon». This prevents the correct use of $I_{630.0}/I_{557.7}$ for determining the type of mid-latitude aurora «because of possible latitudinal spacing of 630.0 and 557.7 nm emission layers». Clarifying this statement, note that it is about the difference between latitudes of emitting regions falling within the SATI-1M field of view at different heights. It is perhaps for this reason the values of $I_{630.0}/I_{557.7} > 10$, characteristic of the SAR arc, were obtained in intervals 3, 4, 5, and 7, although, as shown in Figure 3, *a*, the arc, if emitted at h=400 km, could fall within the spectrograph field of view only in interval 2. Given the above, we do not use the ratio $I_{630.0}/I_{557.7}$ to determine the aurora type, but only compare its time variation with dynamics of magnetospheric-ionospheric disturbances and their manifestations in the MIT structure.

Figure 7, *a* shows that from 14:00 to 15:30 UT the MIT depth increased from 15 to 75 %, and its bottom shifted to φ=52.5°; in fact, to the latitude of GPhO. According to ionospheric sounding data, approximately at the same time, at 15:25 UT (beginning of interval 3), on ionograms there appeared F2s reflections associated with the approach to an observation point of the MIT polar wall; then, at 15:52 UT (end of interval 3), F3s reflections arising in a narrow ionization trough (see Figures 2 and 3, *d*).

At the moment of occurrence of F2s reflections, the MIT polar wall and bottom fell within the SATI-1M field of view at h=200–400 and h=100 km, where in interval 3 the largest synchronous increases in $I_{630.0}$ and $I_{557.7}$ were detected. Figure 9, *a* shows that the strongest peak-shaped increase in the ratio $I_{630.0}/I_{557.7}$ to ~27 occurred in this interval. Smaller increases in $I_{630.0}/I_{557.7}$ to 17 and 12 were found in intervals 5 and 7, in which synchronous bursts of intensities of the emissions considered were also recorded. The MIT latitudinal structure in these intervals differed markedly from that in interval 3 (Figure 9, *c*). In interval 5, due to the expansion of MIT to the north and south the measuring range of I_N and T_N shifted to the MIT bottom; and that of I_S and T_S neared the base of the MIT equatorial wall. In interval 7, the zone of slightly varying TEC values, located between poorly-defined MIT walls, fell within the FPI field of view.

Comparing the plots presented in Figure 9, we can see that the peaks of $I_{630.0}/I_{557.7}$ (Figure 9, *a*), as well as the peaks of I_N/I_Z, $I_N/(2I_Z)$, and I_N/I_S (Figure 9, *b*), were observed in intervals exhibiting enhanced magnetospheric convection (top panel in Figure 9). This refers to
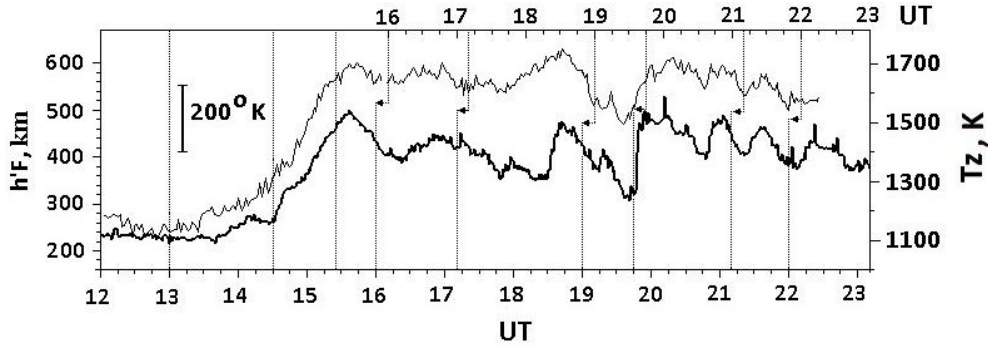
Figure 8. Variations in the minimum virtual height of the ionospheric F-region (black line) and the Doppler temperature over GPhO (gray line)
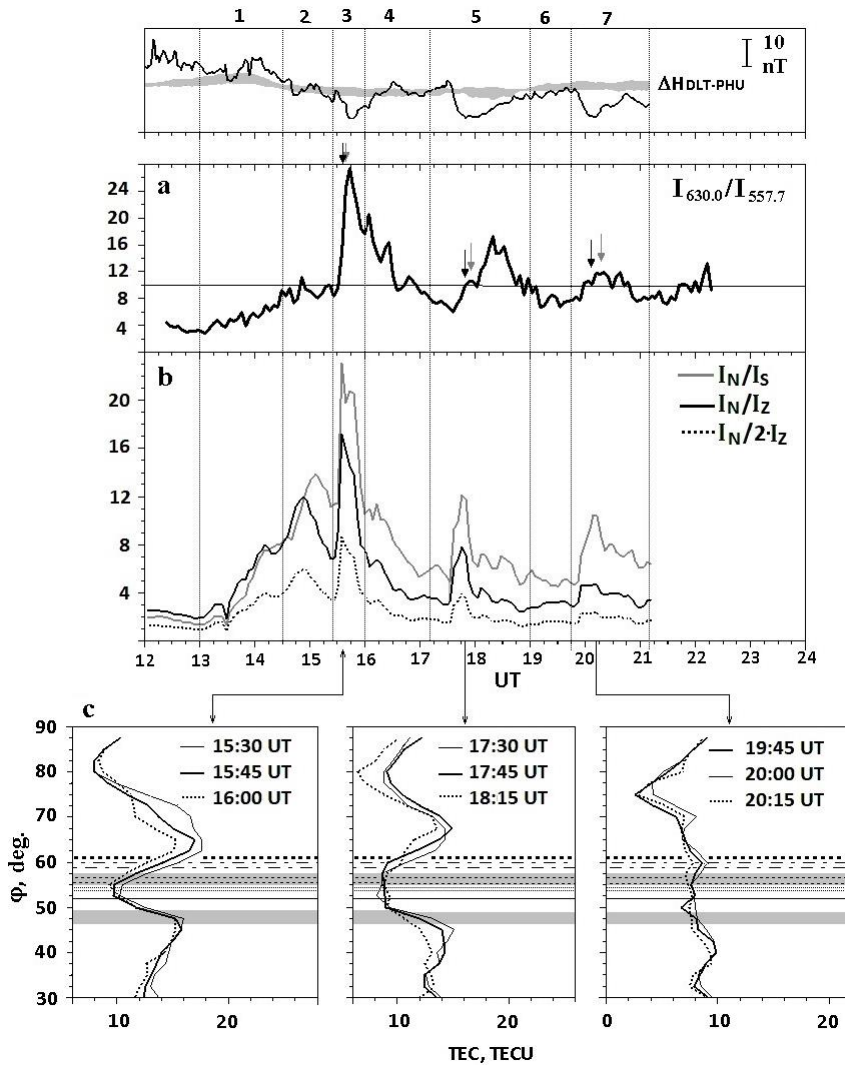

Figure 9. Variations in $I_{630.0}/I_{557.7}$ according to SATI-1M data (*a*) and I_N/I_Z, $I_N/(2I_Z)$, I_N/I_S (*b*), as well as latitudinal TEC profiles in intervals 3, 5, and 7 (*c*). Black and gray arrows denote peaks of bursts of $I_{630.0}$ and $I_{557.7}$. For comparison, the top panel shows variations in $\Delta H_{DLT-PHU}$

the well-known tendency for the 630.0 nm emission intensity to increase with latitude when the magnetospheric convection is enhanced. In intervals 3, 5, and 7, the peaks of $I_{630.0}$ are respectively 3, 6, and 10 min ahead of those of $I_{557.7}$, which might be associated with propagation of the common zone of release of both emissions, excited at different heights, equatorward

when the magnetic convection is enhanced.

The height of the $I_{630.0}/I_{557.7}$ peaks decreases from 27 in interval 3 to 17 and 12 in intervals 5 and 7 respectively. The peaks of I_N/I_Z and I_N/I_S decrease with time too. In interval 5, they are 2.2 and 1.9 and in interval 7, 3.8 and 2.2 times lower than in interval 3. Comparing variations in $I_{630.0}/I_{557.7}$, I_N/I_Z, and I_N/I_S in intervals 3, 5, and 7

with those depicted in Figure 9, *c* shows that the decrease in these ratios over time might have been caused by changes in the latitudinal structure of MIT. The ratios decrease as the MIT width increases, its depth and TEC gradients on the equatorial and polar walls decrease.

Our analysis shows that we should very carefully use the ratio $I_{630.0}/I_{557.7}$ in the case of magnetic storm main phases to determine the type of mid-latitude auroras when $I_{630.0}$ and $I_{557.7}$ are measured at elevation angles much smaller than 90°, i.e. at different latitudes. The greatest difficulties in determining the aurora type arise if an emitting region, probed with optical instruments, is located in the MIT zone.

5. SAR-ARC DYNAMICS

Mikhalev et al. [2018] have demonstrated that, according to preliminary data, near the north horizon of the KEO Sentinel camera's field of view at ~15:30 UT on March 17 an airglow band was formed which, moving equatorward, gradually took the shape of arc. This arc drifted slowly toward the equator at an average (calculated for an emission height of ~400 km) velocity of ~20 m/s, with its structure and intensity varying. The drift velocity and dimensions of this arc matched the SAR-arc parameters reported, for example, in [Ievenko, Alekseev, 2004].

The detailed analysis of latitudinal distributions of the mean 630.0 nm emission intensity in the sector λ=98°–108°, carried out using KEO Sentinel data, has revealed that a structure, defined in [Mikhalev et al., 2018] as SAR arc, appeared on the background of the diffuse emission one hour earlier, at 14:30 UT (21:30 LT), at φ=55.9° N (φ'~51.8°, *L*~3.2). Figure 4, *b* indicates that at that time the depth of the horizontal magnetic component decrease in Yakutsk was equal to that observed in Tiksi. Three hours earlier, at 11:16 UT, the SAR arc emerged eastward of GPhO (at λ≈130°) at approximately the same latitudes (φ'= 52–59°, *L*~2.8–3.8) [Ievenko, Parnikov, 2020]. Figure 3, *a* shows that the SAR arc could be observed with FPI in a northerly direction at 14:30–15:00 UT and at the zenith at ~17:30–19:00 UT.

The plots in Figure 3, *a* and the latitudinal TEC distributions, compared with latitudinal distributions of the 630.0 nm emission intensity (Figure 10), denote that the 630.0 nm emission intensity peak corresponding to the SAR arc originally appeared near the base of the MIT polar wall (Figure 10, *a*). At 15:00–18:00 UT, the SAR arc was in the vicinity of the MIT bottom or near the base of its equatorial wall (Figure 10, *b*); and then, in the range of low TEC values slightly varying with latitude, which has been described in Section 2.2 (panel *d*). At 15:30 UT, the SAR-arc center was at Δφ'~1.2° northward of GPhO; at 17:30–19:00 UT, at the zenith of the observatory. According to our estimates made from KEO Sentinel data, the SAR-arc intensity in the vicinity of the zenith ranged from 100 to 300 R. We believe that the SAR-arc emission contributed to the formation of the I_Z peak at ~18:00 UT (interval 5) — the highest of those observed on March 17, 2015 in the zenith direction.

In most papers it is taken that the formation of a classical SAR arc is driven by the heat inflow from the inner magnetosphere in the plasmapause region (see, e.g., [Mendillo et al., 2016; Ievenko, Parnikov, 2020]). There are, however, studies showing that a SAR arc can also be formed in the polarization jet area and related narrow ionospheric trough [Khalipov et a.l, 1985; Foster et al., 1994; Sazykin et al., 2002; Chu et al., 2019]. The typical lifetime of the narrow ionization trough is 2–3 hr [Stepanov et al., 2017]. The possibility of SAR-arc occurrence in the polarization jet area has also been discussed in [Sazykin et al., 2002]. The model calculations cited therein show that in these cases a weak arc is formed due to frictional heating of the atmosphere, which leads to an increase in the rate of dissociative recombination and to the probability of excitation of oxygen atoms in the ^{1}D state when colliding with thermal electrons. The arcs associated with the polarization jet differ from classical SAR arcs in low intensity, short lifetime, and in that they appear without significant heat inflow from the upper layers of the magnetosphere.

Several SAR arcs from different sources may exist at a time. Simultaneous detection of two or more SAR arcs was mentioned, for example, in [Ievenko et al., 2008; Hong et al., 2020]. Ievenko et al. [2008] associate the second SAR arc with the residual plasmapause. In the case we deal with, the F3s reflections indirectly indicating the presence of a narrow ionization trough near GPhO occurred at 15:52–19:00 UT (see Section 2.3.). The second SAR arc was occasionally observed from 16:00 to 19:50 UT, i.e. it appeared 68 min later than the F3s reflections and existed for 50 min after their disappearance. An example of the latitudinal distribution of the 630.0 nm emission intensity with two peaks, located southward of the MIT polar wall, is given in Figure 10, *c*. The short lifetime of the second SAR arc in our case may indicate an ionospheric source of its formation associated with the polarization jet [Sazykin et al., 2002].

There was a single SAR arc in the images captured at GPhO before the end of observations (~22:30 UT, 05:30 LT). By that time, it had shifted to φ=49.7° N (φ'~45.6°, *L*~2). In ~1.5 hrs, the presence of a SAR arc on *L*~2.35–2.5 was detected in the Western Hemisphere in Millstone Hill (φ=42.6° N, λ=71.4° W; φ'= 52.5°) [Hong et al., 2020]. The SAR arc was observed there for the entire period of optical measurements, made on March 18 from 00:06 to 09:47 UT (19:00–05:00 LT) during the storm recovery phase. Hong et al. [2020] have demonstrated that the SAR arc they observed was classical, formed by heat inflow from the inner magnetosphere.

Thus, according to the literature sources and our research, during the March 17–18, 2015 storm the SAR arc existed for more than 23 hrs. It appeared 5 hrs after the onset of the storm main phase and was observed until the end of the main phase and at least for 10.5 hr of the recovery phase. We believe that as the storm developed the role of heat inflows from the region of interaction of the ring current with the plasmasphere gradually increased and became dominant after 19:00 UT on 17 March.

RESULTS

The comprehensive analysis of geomagnetic, ionospheric, and optical phenomena has identified peculiarities of the 557.7 and 630.0 nm atomic oxygen emissions
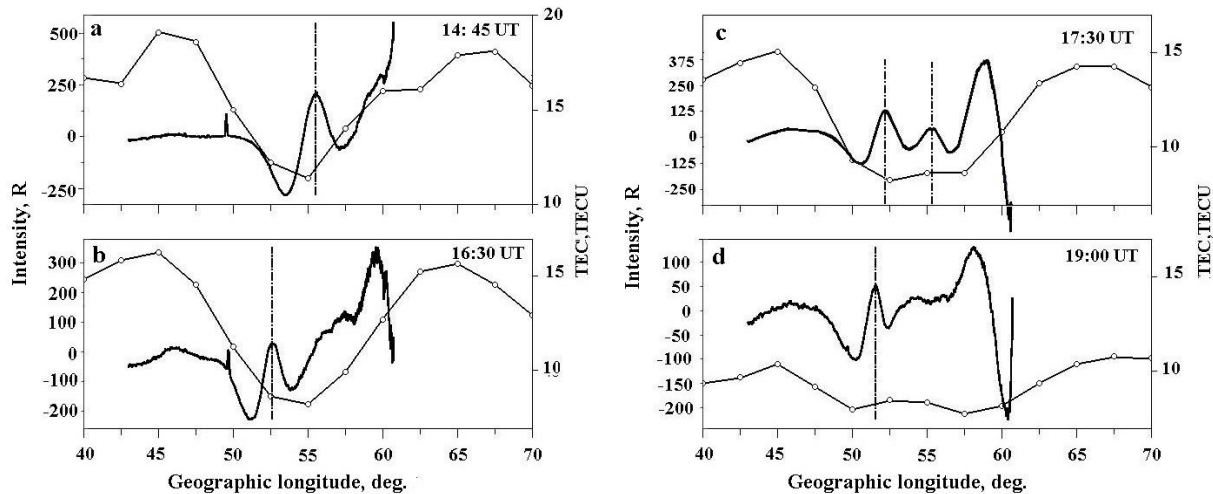
Figure 10. Latitudinal distributions of TEC (line with circles) and deviations of the 630.0 nm emission intensity in the SAR-arc center (solid line) from a component slowly varying with latitude (derived from KEO Sentinel images). The slowly varying component was separated from initial data by smoothing it by a running mean over 55 points. The time series remaining after its elimination were smoothed over 11 points. The intensity values obtained in the 98–108° E sector were averaged. The calculation was made for h=400 km. Vertical dash-dotted lines denote the latitude of intensity peaks of stable arcs

observed at the ISTP SB RAS Geophysical Observatory at 12:00–22:30 UT on March 17, 2015 during a magnetic storm.

We have shown that strengthenings of the westward electrojet occurred with an increase in the 630.0 nm emission intensity at all latitudes falling within fields of views of the instruments in hand. The increase in the 630.0 nm emission intensity was accompanied by a rise in the Doppler temperature in the cases when in the space-fixed field of view of a device were latitudes of the MIT equatorial wall or bottom.

The greatest synchronous 557.7 and 630 nm emission intensity increases were detected during three activations of the westward electrojet, which developed as the magnetospheric convection was enhanced.

We have found out that $I_{630.0}/I_{557.7}$ and the ratios between the 630.0 nm emission intensities observed in the north, zenith, and south directions depend on the position of emitting regions in these directions relative to the MIT bottom. Peaks of the ratios were maximum at 15:25–16:00 UT, when the 630.0 nm emission intensities in the north direction were recorded at latitudes of the MIT polar wall; the 630.0 nm emission intensities in the zenith and south directions and the 557.7 nm emissions, at latitudes of the MIT bottom and equatorial wall. The peak values decreased after latitudes of the MIT bottom fell within the devices' fields of view in a northerly direction, and went down to minimum when all the intensities were measured in the range of slightly varying small TEC values.

The SAR arc was found to appear at latitudes of the base of the MIT polar wall when the westward electrojet center began to move equatorward. Then the arc shifted to the latitudes of the MIT bottom and the base of its equatorial wall located near GPhO that time. In the vicinity of the zenith, the SAR-arc intensity varied from 100 to 300 R.

It is shown that 68 min after the appearance of F3s reflections on ionograms, the second, weaker arc, located

by 2.5–3.0° northward of the main one, became visible in the images captured by the all-sky camera. Judging by the presence of the F3s reflections, the primary source of the second arc might have been a polarization jet associated with a narrow ionospheric trough. The presence of two stable auroral red arcs spaced in latitude suggests the possibility of simultaneous existence of two SAR-arc sources differing in heating processes that occur in them.

Let us stress that the above results have been obtained from a study of only one strong storm and their repeatability should be checked against other magnetic storms.

REFERENCES

Alekseev V.N., Velichko V.A., Nadubovich Yu.A. Study of the glow heights and the position of the southern boundary of the background glow of 6300 Å. *Fizika verkhney atmosfery vysokikh shirot* [Physics of the Upper Atmosphere of High Latitudes]. Yakutsk, YaB of SB AS USSR Publ., 1975, vol. 3, pp. 124–133. (In Russian).

Aruliah A., Förster M., Hood R., McWhirter I., Doornbos E. Comparing high-latitude thermospheric winds from Fabry–Perot interferometer (FPI) and challenging mini-satellite payload (CHAMP) accelerometer measurements. *Ann. Geophys*. 2019, vol. 37, pp. 1095–1120. DOI: 10.5194/angeo-37-1095-2019.

Balan N., Shiokawa K., Otsuka Y., Kikuchi T., Lekshmi D.V., Kawamura S., Yamamoto M., Bailey G.J. A physical mechanism of positive ionospheric storms at low latitudes and midlatitudes. *J. Geophys. Res.* 2010, vol. 115, A02304. DOI: 10.1029/2009JA014515.

Bame S.J., Asbridgie J.R., Felthauseer H.E., Honesa E.W., Strong I.B. Characteristics of the plasma sheet in the Earth's magnetotail. *J. Geophys. Res.* 1967, vol. 72, iss. 1, pp. 113–129. DOI: 10.1029/JZ072i001p00113.

Baumjohann W., Paschmann G., Cattell C.A. Average plasma properties in the central plasma sheet. *J. Geophys. Res.* 1989, vol. 94, iss. 6, pp. 6597–6606. DOI: 10.1029/JA094iA06p06597.

Blanc M., Richmond A.D. The ionospheric disturbance dynamo. *J. Geophys. Res.*, 1980, vol. 85, iss. A4, pp. 1669–1686. DOI: 10.1029/JA085iA04p01669.

Bryunelli B.E., Namgaladze A.A. *Fizika ionosfery* [Physics of ionosphere]. Moscow, Nauka Publ., 1988, 528 p. (In Russian).

Chu X., Malaspina D., Gallardo-Lacourt B., Liang J., Andersson L., Ma Q., Artemyev A., Liu J., Ergun R.E., Thaller S., Akbari H., Zhao H., Larsen B., Reeves G., Wygant J., Breneman A., Tian S., Connors M., Donovan E., Archer W., MacDonald E.A. Identifying STEVE's magnetospheric driver using conjugate observations in the magnetosphere and on the ground. *Geophys. Res. Lett.* 2019, vol. 46, iss. 22, pp. 12665–12674.

Deminov M.G. Ionosphere of the Earth: Features and Mechanisms. *Elektromagnitnye i plazmennye protsessy ot nedr Solntsa do nedr Zemli. Yubileinyi sbornik IZMIRAN-75* [Electromagnetic and Plasma Processes from the Interior of the Sun to the Interior of the Earth. Jubilee Collection IZMIRAN-75]. Moscow, 2015, pp. 295–346. (In Russian).

Deminov M.G., Shubin V.N. Empirical model of the location of the main ionospheric trough. *Geomagnetism and Aeronomy.* 2018, vol. 58, iss. 3, pp. 338–347. DOI: 10.1134/S0016793218030064.

Ding G.-X., He F., Zhang X.-X., Chen B. A new auroral boundary determination algorithm based on observations from TIMED/GUVI and DMSP/SSUSI. *J. Geophys. Res.* 2017, vol. 122, pp. 2162–2173. DOI: 10.1002/2016JA023295.

Feldstein Y.I., Vorobjev V.G., Zverev V.L. Planetary features of aurorae: Results of the IGY (a review). *Geomagnetism and Aeronomy.* 2010, vol. 50, no. 4, pp. 413–435. DOI: 10.1134/S0016793210040018.

Feldstein Y.I., Vorobjev V.G., Zverev V.L., Förster M. Investigations of the auroral luminosity distribution and the dynamics of discrete auroral forms in a historical retrospective. *History Geo-Space Sci.* 2014, vol. 5, pp. 81–134. DOI: 10.5194/hgss-5-81-2014.

Filippov V.M., Shestakova L.V., Galperin Y.I. Fast ion drift band in the subauroral F-region and its manifestation in the structure of the high-latitude ionosphere. *Kosmicheskie issledovaniya* [Cosmic Research]. 1984, vol. 27, no. 4, pp. 557–564. (In Russian).

Foster J.C., Buonsanto M.J., Mendillo M., Nottingham D., Rich F.J., Denig W. Coordinated stable auroral red arc observations: Relationship to plasma convection. *J. Geophys. Res.* 1994, vol. 99, pp. 11,429–11,439.

Frey H.U. Localized aurora beyond the auroral oval. *Rev. Geophys.* 2007, vol. 45, RG1003. DOI: 10.1029/2005RG000174.

Gonzalez W.D., Tsurutani B.T., Lepping R.P., Schwenn R. Interplanetary phenomena associated with very intense geomagnetic storms. *J. Atmos. Solar-Terr. Phys.* 2002, vol. 64, pp. 173–181.

Gussenhoven M.S., Hardy D.A., Heinemann N. Systematics of the equatorward diffuse auroral boundary. *J. Geophys. Res.* 1983, vol. 88, iss. A7, pp. 5692–5708.

Hairston M., Coley W.R., Stoneback R. Responses in the polar and equatorial ionosphere to the March 2015 St. Patrick Day storm. *J. Geophys. Res.* 2016, vol. 121, pp. 11,213–11,234. DOI: 10.1002/2016JA023165.

He M., Liu L., Wan W., Zhao B. A study on the nighttime midlatitude ionospheric trough. *J. Geophys. Res.*, 2011, vol. 116, iss. A5, A05315. DOI: 10.1029/2010JA016252.

Hong J., Kim Y.H., Kam H., Chung J.-K., Park J., Kim J.-H., Mendillo M. Simultaneous observations of SAR arc and its ionospheric response at subauroral conjugate points ($L \approx 2.5$) during the St. Patrick's Day Storm in 2015. *J. Geophys. Res.* 2020, vol. 124, iss. 4. DOI: 10.1029/2019JA027321.

Ievenko I.B., Alekseev V.N. Effect of the substorm and storm on the sar arc dynamics: A statistical analysis. *Geomagnetism and Aeronomy.* 2004, vol. 44, no. 5, pp. 592–603.

Ievenko I.B., Parnikov S.G., Alexeyev V.N. Relationship of the diffuse aurora and SAR arc dynamics to substorms and storms. *Adv. Space Res.* 2008, vol. 41, no. 8, pp. 1252–1260. DOI: 10.1016/j.asr.2007.07.030.

Ievenko I.B., Parnikov S.G. Ground-based and satellite observations of the SAR-arc in the MLT evening sector at the beginning of the magnetic storm on March 17, 2015. *Geomagnetism and Aeronomy.* 2020, vol. 60, no 6, pp. 737–746. DOI: 10.1134/S0016793220050096.

Jacobsen K.S., Andalsvik Y.L. Overview of the 2015 St. Patrick's Day storm and its consequences for RTK and PPP positioning in Norway. *J. Space Weather Space Climate.* 2016, vol. 6, A9. DOI: 10.1051/swsc/2016004.

Keika K., Nakamura R., Baumjohann W., Angelopoulos V., Chi P.J., Glassmeier K.H., Fillingim M., Magnes W., Auster H.U., Fornacon K.H., Reeves G. D., Yumoto K., Lucek E.A., Carr C.M., Dandouras I. Substorm expansion triggered by a sudden impulse front propagating from the dayside magnetopause. *J. Geophys. Res.* 2009, vol. 114, A00C24. DOI: 10.1029/2008JA013445.

Khalipov V.L., Sivtseva L.D., Filippov V.M., Stepanov A.E., Nikolaenko L.M., Bosqued J.M., Beghin C. Step-like profiles of electron density in the subauroral lower F-region in the morning sector and possible mechanisms of their formation during substorms: the comparison of data of ground-based ionosondes with the AUREOL-3 satellite measurements. *Results of the ARCAD 3 project and of the recent programmes in magnetospheric and ionospheric physics, Toulouse, 1984.* Toulouse, Cepadues-editions, 1985, pp. 895–916.

Khalipov V.L., Stepanov A.E., Ievenko I.B., Kotova G.A., Panchenko V.A. Formation of red arc in the polarization jet band. *J. Atmos. Solar-Terr. Phys.* 2018, vol. 179, pp. 494–503. DOI: 10.1016/j.jastp.2018.08.005.

Khomich V.Yu., Semenov A.I., Shefov N.N. *Airglow as an Indicator of Upper Atmospheric Structure and Dynamics.* Springer-Verlag Berlin Heidelberg, 2008, 756 p.

Kosar B.C., MacDonald E.A., Case N.A., Zhang Y., Mitchell E.J., Viereck R. A case study comparing citizen science aurora data with global auroral boundaries derived from satellite imagery and empirical models. *J. Atmos. Solar-Terr. Phys.* 2018, vol. 177, pp. 274–282. DOI: 10.1016/j.jastp.2018.05.006.

Le G., Lühr H., Anderson B.J., Strangeway R.J., Russell C.T., Singer H., Slavin J.A., Zhang Y., Huang T., Bromund K., Chi P.J., Lu G., Fischer D., Kepko E.L., Leinweber H.K., Magnes W., Nakamura R., Plaschke F., Park J., Rauberg J., Stolle C., Torbert R.B. Magnetopause erosion during the March 17, 2015 magnetic storm: Combined field-aligned currents, auroral oval, and magnetopause observations. *Geophys. Res. Lett.* 2016, vol. 43, iss. 4, pp. 2396–2404. DOI: 10.1002/ 2016GL068257.

McPherron R.L. The use of ground magnetograms to time the onset of magnetospheric substorms. *Journal of Geomagnetism and Geoelectricity.* 1978, vol. 30, pp.149–163.

Megan Gillies D., Knudsen D., Donovan E., Jackel B., Gillies R., Spanswick E. Identifying the 630 nm auroral arc emission height: A comparison of the triangulation, FAC profile, and electron density methods. *J. Geophys. Res.* 2017, vol. 122, pp. 8181–8197. DOI: 10.1002/2016JA023758.

Mendillo M. Storms in the ionosphere: Patterns and processes for total electron content. *Rev. Geophys*. 2006, vol. 44, iss. 4, RG4001. DOI: 10.1029/2005RG000193.

Mendillo M., Baumgardner J., Wroten J., Martinis C., Smith S., Merenda K.D., Fritz T., Hairston M., Heelis R., Barbieri C. Imaging magnetospheric boundaries at ionospheric heights. *J. Geophys. Res.* 2013, vol. 118, iss. 11, pp. 7294–7305. DOI: 10.1002/2013JA019267.

Mendillo M., Finan R., Baumgardner J., Wroten J., Martinis C., Casillas M. A stable auroral red (SAR) arc with multiple emission features. *J. Geophys. Res*. 2016, vol. 121, pp. 10,564–10,577. DOI: 10.1002/2016JA023258.

Meurant M., Gerard J.-C., Blockx C., Hubert B., Coumans V. Propagation of electron and proton shock-induced aurora and the role of the interplanetary magnetic field and solar wind *J. Geophys. Res*. 2004, vol. 109, A10210. DOI: 10.1029/2004JA010453.

Mikhalev A.V. Mid-latitude aurora in solar cycles 23–24 from observations in the south of Eastern Siberia. *Solar-Terr. Phys.* 2019, vol. 5, iss. 4, pp. 66–73. DOI: 10.12737/stp-54201909.

Mikhalev A.V., Beletsky A.B., Vasilyev R.V., Zherebtsov G.A., Podlesny S.V., Tashchilin M.A., Artamonov M.F. Spectral and photometric characteristics of mid-latitude auroras during the magnetic storm of March 17, 2015. *Solar-Terr. Phys.* 2018, vol. 4, iss. 4, pp. 42–47. DOI: 10.12737/ stp-44201806.

Mishin V.V., Lunyushkin S.B., Mikhalev A.V., Klibanova Yu.Yu., Tsegmed B., Karavaev Yu.A., Tashchilin A.V., Leonovich L.A., Penskikh Yu.V. Extreme geomagnetic and optical disturbances over Irkutsk during the 2003 November 20 superstorm. *J. Atmos. Solar-Terr. Phys*. 2018, vol. 181, pt. A, pp. 68–78. DOI: 10.1016/j.jastp.2018.10.013.

Moldwin M.B., Downward L., Rassoul H.K., Amin R.R., Anderson R.R. A new model of the location of the plasmapause: CRRES results. *J. Geophys. Res*. 2002, vol. 107, iss. A11, pp. SMP 2-1–SMP 2-9. DOI: 10.1029/2001JA009211.

Nagai T., Baker D.N., Higbie P.R. Development of substorm activity in multiple-onset substorms at synchronous orbit. *J. Geophys. Res*. 1983, vol. 88, iss. A9, pp. 6994–7004.

Newell P.T., Sotirelis T., Wing S. Diffuse, monoenergetic, and broadband aurora: The global precipitation budget. *J. Geophys. Res*. 2009, vol. 114, A09207. DOI: 10.1029/2009JA014326.

Ni B., Thorne R.M. Zhang X., Bortnik J., Pu Z., Xie L., Hu Z., Han D., Shi R., Zhou C., Gu X. Origins of the Earth's Diffuse Auroral Precipitation. *Space Sci Rev*. 2016, vol. 200, pp. 205–259. DOI: 10.1007/s11214-016-0234-7.

Podlesnyi A.V., Brynko I.G., Kurkin V.I., Berezovsky V.A., Kiselyov A.M., Petuchov E.V.Multifunctional chirp ionosonde for monitoring the ionosphere. *Geliogeofizicheskie issledovaniya* [Heliogeophysical Research]. 2013, iss. 4, pp. 24–31. Available at: http://vestnik.geospace.ru/index.php?id=166 (Accessed 10 November 2020). (In Russian).

Polekh N., Zolotukhina N., Kurkin V., Zherebtsov G., Shi J., Wang G., Wang Z. Dynamics of ionospheric disturbances during the 17–19 March 2015 geomagnetic storm over East Asia. *Adv. Space Res.* 2017, vol. 60, iss. 11, pp. 2464–2476. DOI: 10.1016/j.asr.2017.09.030.

Polekh N.M., Zolotukhina N.A., Romanova E.B., Ponomarchuk S.N., Kurkin V.I., Podlesnyi A.V. Ionospheric effects of magnetospheric and thermospheric disturbances on March 17–19, 2015. *Geomagnetism and Aeronomy*. 2016, vol. 56, no. 5, pp. 557–571. DOI: 10.1134/S0016793216040174.

Pryse S.E., Kersley L., Malan D., Bishop G.J. Parameterization of the main ionospheric trough in the European sector. *Radio Sci.* 2006, vol. 41, RS5S14. DOI: 10.1029/2005RS003364.

Rassoul H.K., Rohrbaugh R.P., Tinsley B.A., Slater D.W. Spectrometric and photometric observations of low-latitude aurorae. *J. Geophys. Res.* 1993, vol. 98, iss. A5, pp. 7695–7709. DOI: 10.1029/92JA02269.

Sazykin S., Fejer B.G., Galperin Yu.I., Zinin L.V., Grigoriev S.A., Mendillo M. Polarization jet events and excitation of weak SAR arcs. *Geophys. Res. Lett.* 2002, vol. 29, iss. 12, pp. 26-1–26-4. DOI: 10.1029/2001GL014388.

Shinbori A., OtsukaY., Tsugawa T., Nishioka M., Kumamoto A., Tsuchiya F., Matsuda S., Kasahara Y., Matsuoka A., Ruohoniemi J.M., Shepherd S.G., Nishitani N. Temporal and spatial variations of storm time midlatitude ionospheric trough based on global GNSS-TEC and Arase satellite observations. *Geophys. Res. Lett.* 2018, vol. 45, pp. 7362–7370. DOI: 10.1029/2018GL078723.

Shiokawa K., Ogawa T., Kamide Y. Low-latitude auroras observed in Japan: 1999–2004. *J. Geophys. Res.* 2005, vol. 110, A05202. DOI: 10.1029/2004JA010706.

Shindin A.V., Klimenko V.V., Kologin D.A., Beletsky A.B., Grach S.M., Nasyrov I.A., Sergeev E.N. Spatial characteristics of the 630-nm artificial airglow generation region during the Sura facility pumping. *Radiophysics and Quantum Electronics.* 2018, vol. 60, no. 11, pp. 849–865. DOI: 10.1007/s11141-018-9852-0.

Suzuki H., Chino H., Sano Y., Kadokura A., Ejiri M.K., Taguchi M. Imaging-based observations of low-latitude auroras during 2001–2004 at Nayoro, Japan. *Earth, Planets and Space.* 2015, vol. 67, 107. DOI: 10.1186/s40623-015-0278-z.

Starkov G.V. *Planetarnaya dinamika avroral'nogo svecheniya. Fizika okolozemnogo kosmicheskogo prostranstva. T. 1* [Planetary Dynamics of the Aurora. Physics of Near-Earth Space. Vol. 1]. Apatity, Publishing House of the Kola Scientific Center of RAN, 2000, 706 p. (In Russian).

Stepanov A.E., Khalipov V.L., Golikov I.A., Bondar E.D. *Polyarizatsionnyi dzhet: uzkie i bystrye dreify subavroral'noi ionosfernoi plazmy* [Polarization Jet: Narrow and Fast Drifts of Subauroral Ionospheric Plasma]. Yakutsk, Publishing House of the NEFU, 2017, 176 p. (In Russian).

Tashchilin A.V., Leonovich L.A. Modeling nightglow in atomic oxygen red and green lines under moderate disturbed geomagnetic conditions at midlatitudes. *Solar-Terr. Phys.* 2016, vol. 2, iss. 4, pp. 94–106. DOI: 10.12737/24276.

Tsurutani B.T., Lakhina G.S., Verkhoglyadova O.P., Gonzalez W.D., Echer E., Guarnieri F.L. A review of interplanetary discontinuities and their geomagnetic effects. *J. Atmos. Solar-Terr. Phys.* 2011, vol. 73, pp. 5–19. DOI: 10.1016/j.jastp. 2010.04.001.

Vasilyev R.V., Artamonov M.F., Beletsky A.B., Zherebtsov G.A., Medvedeva I.V., Mikhalev A.V., Syrenova T.E. Registering upper atmosphere parameters in East Siberia with Fabry—Perot Interferometer KEO Scientific "Arinae". *Solar-Terr. Phys.* 2017, vol. 3, iss. 3, pp. 61–75. DOI: 10.12737/stp-33201707.

Zherebtsov G.A., Pirog O.M., Razuvayev O.I. The high-latitude ionosphere structure and dynamics. *Issledovaniya po geomagnetizmu, aeronomii i fizike Solntsa* [Research on Geomanetism, Aeronomy and Solar Physics]. 1986, iss. 76, pp. 165–177. (In Russian).

Zolotukhina N.A., Kurkin V.I., Polekh N.M., Romanova E.B. Backscattering dynamics during intense geomagnetic storm as deduced from Yekaterinburg radar data: 17–22 March 2015. *Solar-Terr. Phys.* 2016, vol. 2, iss. 4, pp. 31–54. DOI: 10.12737/24272.

Zolotukhina N., Polekh N., Kurkin V., Rogov D., Romanova E., Chelpanov M. Ionospheric effects of St. Patrick's storm over Asian Russia: 17–19 March 2015. *J. Geophys. Res.* 2017, vol. 122, pp. 2484–2504. DOI: 10.1002/2016JA023180.

Zverev V.L., Feldstein Y.I., Vorobjev V.G. Auroral glow equatorward from the auroral oval. *Geomagnetism and Aeronomy*. 2012, vol. 52, no. 1, pp. 60–67. DOI: 10.1134/S0016793212010173.

URL: https://www.swpc.noaa.gov/noaa-scales-explanation (accessed April 2, 2021).

URL: https://www.intermagnet.org/data-donnee/download-eng.php (accessed October 16, 2015).

URL: ftp.swpc.noaa.gov/pub/warehouse (accessed October 15, 2015).

URL: https://www.ngdc.noaa.gov/stp/ovation_prime/data (дата обращения March 20, 2020).

URL: http://ckprf.ru/ckp/3056 (accessed April 15, 2015).

URL: www.intermagnet.org (accessed March 21, 2015).

URL: http://cdaweb.gsfc.nasa.gov/istp_public (accessed July 15, 2015).